ACS OMEGA

http://pubs.acs.org/journal/acsodf

Article

Computation and Investigation of Two-Dimensional $WO_3 \cdot H_2O$ Nanoflowers for Electrochemical Studies of Energy Conversion and Storage Applications

Phuoc Anh Le,* Van Qui Le, Thien Lan Tran, Nghia Trong Nguyen, and Thi Viet Bac Phung*

Cite This: *ACS Omega* 2022, 7, 10115−10126

Read Online

ACCESS | Metrics & More | Article Recommendations

ABSTRACT: The aim of this study is to prepare a two-dimensional (2D) $WO_3 \cdot H_2O$ nanostructure assembly into a flower shape with good chemical stability for electrochemical studies of catalyst and energy storage applications. The 2D-$WO_3 \cdot H_2O$ nanoflowers structure is created by a fast and simple process at room condition. This cost-effective and scalable technique to obtain 2D-$WO_3 \cdot H_2O$ nanoflowers illustrates two attractive applications of electrochemical capacitor with an excellent energy density value of 25.33 W h kg^{-1} for high power density value of 1600 W kg^{-1} and good hydrogen evolution reaction results (low overpotential of 290 mV at a current density of 10 mA cm^{-2} with a low Tafel slope of 131 mV dec^{-1}). A hydrogen evolution reaction (HER) study of WO_3 in acidic media of 0.5 M H_2SO_4 and electrochemical capacitor (supercapacitors) in 1 M Na_2SO_4 aqueous electrolyte (three electrode system measurements) demonstrates highly desirable characteristics for practical applications. Our design for highly uniform 2D-$WO_3 \cdot H_2O$ as catalyst material for HER and active material for electrochemical capacitor studies offers an excellent foundation for design and improvement of electrochemical catalyst based on 2D-transition metal oxide materials.

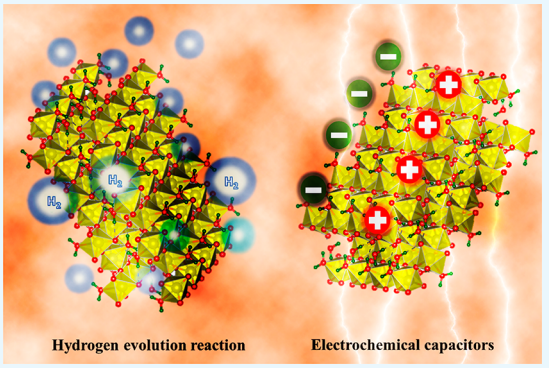

1. INTRODUCTION

In order to overcome the fossil fuels crisis and global warming, it is necessary to provide new, sustainable energy storage and conversion applications.[1] Transition metal oxides (TMOs) have been studied widely during the past few decades in various areas of energy storage, especially batteries and supercapacitor electrodes which enhance the energy density to provide high performance.[2−4] Currently, with the appearance of two-dimensional (2D) nanomaterial, there are many types of 2D materials being applied for both energy storage (supercapacitors) and conversion (electrocatalyst—hydrogen evolution reaction).[5−10] In this condition, the 2D structures of transition metal oxides are attractive due to abundant reserves, ease of synthesis, large surface area, and high-exposure active sites and short ions diffusion distance.[11−14] Herein, in this report, 2D-$WO_3 \cdot H_2O$ with nanoflowers structure is synthesized, studied, and introduced as a good TMO material for dual applications of energy storage and conversion.

Hydrogen production from water splitting through electrocatalysis process has been determined as a clean and sustainable energy source with very high gravimetric power and energy density, zero carbon dioxide emission, and renewability.[15−18] Among various hydrogen production technologies, water splitting by electrocatalytic process is considered as a green way to product hydrogen gas with a simple system, low cost, and abundant raw electrolyte (the pollution water can be used as electrolyte for hydrogen production).[19−21] Herein, the hydrogen reaction is one of the two halves of two reactions in water splitting electrode reactions by the oxygen evolution reaction (OER) and the hydrogen evolution reaction (HER), at the anode and at the cathode, respectively, which can be storage separately for further applications.[22−24] Traditionally, the nobel metal family, especially platinum (Pt), is the best choice for electrocatalyst with strongest reaction kinetics, with lower overpotential and Tafel slope, a mandatory requirement for HER.[25−27] But the noble metal family faces a major problem of high price, shortage and high cost to treat after release,[28,29] so that scientists have been studying ways to replace them by the other low-cost and abundant materials. Currently, transition metal oxide materials have been increasing as promising candidates for HER studies due to good performance, low cost, earth-

Received: November 2, 2021
Accepted: March 3, 2022
Published: March 16, 2022

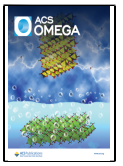

Table 1. Lattice Constants

$WO_3·H_2O$	a (Å)	b (Å)	c (Å)	α	β	γ
GGA	5.3444	10.2471	5.0485	90.000	91.8493	90.000
HSE06	5.3041	10.2219	5.0124	90.000	91.4884	90.000
experiment[48]	5.249	10.711	5.133	NA	NA	NA
experiment[49]	5.2516	10.4345	5.1380	NA	NA	NA

abundance, and easy synthesis.[30−34] Recent advances in transition metal oxide materials have shown that two-dimensional transition metal oxides, especially 2D-$WO_3·H_2O$, would be promising, inexpensive alternatives to high-cost materials for electrochemical catalyst application.

Currently, TMO materials also have been studied in electrochemical energy storage applications which include batteries and supercapacitors. As a new energy storage field, supercapacitors are highly attractive for their rapid charge−discharge capability and long life cycle.[35,36] In comparison with various types of materials for supercapacitor electrodes, TMOs are good candidates with many advantages, such as improving the performance by Faradaic reaction at the electrode layer during the charge−discharge process, easy scaling, and sustainability.[37,38] Among various types of TMO materials, tungsten oxide is an excellent choice for a high-exposure active surface, strong durability, and low cost, which are suitable for surpercapacitor electrode and the negative electrode of water splitting.[39,40]

In this work, to widen the field research of $WO_3·H_2O$ as a promising material for various applications, we introduce an excellent method to synthesize 2D-$WO_3·H_2O$. Herein, 2D-$WO_3·H_2O$ was prepared by a fast and simple wet chemical method to obtain a two-dimensional nanoflowers structure which is considered as a versatile active material for energy conversion of hydrogen evolution reaction and energy storage of supercapacitors applications. Furthermore, the complex devices which combine the supercapacitors and hydrogen evolution/oxygen evolution reaction provide an excellent idea of future electrochemical models. Finally, in this report, we will discuss how new computational and experimental techniques were combined with strategies on the understanding of electrochemical capacitor and HER kinetics with the situation of 2D-$WO_3·H_2O$ nanoflowers.

2. RESULTS AND DISCUSSION

2.1. Computational Results of $WO_3·H_2O$ Nanoflowers.

2.1.1. Computational Details. The crystalline structure of $WO_3·H_2O$ nanoflowers is the orthorhombic. To well understand the orthorhombic $WO_3·H_2O$ structure, morphology, and electronic properties, herein, the density functional theory (DFT) calculations were studied by Vienna ab initio Simulation Package (VASP) code.[44,45] Furthermore, the investigation of the electron−ion interactions and electronic exchange correlations was carried out by the projector augmented-wave potentials (PAWs) and the Perdew−Burke−Ernzerhof (PBE) generalized gradient approximation (GGA) functional.[46,47] For comparison purposes, GGA and HSE06 methods were used to reduce the self-interaction error. More importantly, this selectively adds an energy correction to localized electron states such as d or f orbitals that the self-interaction is notably large. Then, the conjugate gradient diagram was chosen in order to optimize all atomic positions and lattice constants until the force components on each atom have the order of 10^{-4} eV $Å^{-1}$. The kinetic energy of the plane-wave basis set cutoff is set as 400 eV to ensure the exactitude of the simulation results. We used the bulk supercell of $WO_3·H_2O$ containing 28 (W/O/H, ∼4/16/8) atoms, which correspond to 4 $WO_3·H_2O$ units. Herein, for the $WO_3·H_2O$ supercell, the numbers of K-mesh were (4 × 2 × 4).

2.1.2. Crystal Structure. The optimized lattice constants of $WO_3·H_2O$ were obtained from our DFT calculations are shown in Table 1; experimental values are included for comparison. The stable structure of $WO_3·H_2O$ calculated using the GAA method show the lattice parameters values of a = 5.3444, b = 10.2471, and c = 5.0485 Å, which corresponded correctly with published data of $WO_3·H_2O$ X-ray diffraction (JCPDS Card No.43-0679) and the American Mineralogist Crystal Structure Database (AMCSD 0005199).[48] According to the results described in Table 1, the functional GGA and HSE06 provide accurate description of the lattice parameters of $WO_3·H_2O$.

Herein, the crystal structure of $WO_3·H_2O$ sheets is made by the basic structural unit of a [WO_5−H_2O] octahedron with the location of W at the center of an octahedron and connection to six oxygen atoms by a W−O covalent bond. The sheets are stacked in the direction of [010] with the intercalation with each other by a hydrogen bond (O−H···O) which forms a three-dimensional network structure. Protons (hydrogen atoms) are marked in green, red for oxygen ions, and yellow for tungsten ions and also WO_6 octahedral.

$WO_3·H_2O$ crystallizes in the orthorhombic *Pnma* space group. The crystal structure of 2D-$WO_3·H_2O$ nanosheets (Figure 1) is made by the basic structural unit of a [WO_5−H_2O] octahedron, with the location of W atom in the center of an octahedron which connected to six oxygen atoms by a W−O covalent bond. There is a spread of W−O bond distances ranging from 1.753 to 1.943 Å. The six corners are made by six oxygen atoms of the octahedron can be classified into three types: (1) the oxygen atom (O_1) locate in H_2O, (2) two vertices of the octahedron is made by one another oxygen atom (O_2), and (3) four locations at four corners of the same plane are four oxygen atoms (O_3) and form a rectangle perpendicular to the [010] direction. The O_1 atom at the upper vertex of the octahedron bond shares corner mode with four O_3 atoms to four adjacent the octahedron with the upper vertex as the O_2 atom, respectively. Herein, the three-dimensional network structure is made from sheets intercalating with each other by a hydrogen bond (O_1−H···O_2) and stack in the direction of [010].

2.1.3. Electronic Structures. Density of states (DOS) and electronic energy band structures of $WO_3·H_2O$ are calculated with the functional GGA and HSE06. The results are presented in Figures 2 and 3. The energy band gap of $WO_3·H_2O$ has been calculated by the following equation: $E_g = E_{VB} - E_{CB}$ (where E_{VB} and E_{CB} respectively represent potential energy of valence band (VB) and conduction band (CB)). $WO_3·H_2O$ has relatively small band gap and is widely studied. The calculated electronic density of states DOS of $WO_3·H_2O$ using GGA method is shown on the right-hand side in Figure 2 with

https://doi.org/10.1021/acsomega.1c06150
ACS Omega 2022, 7, 10115−10126

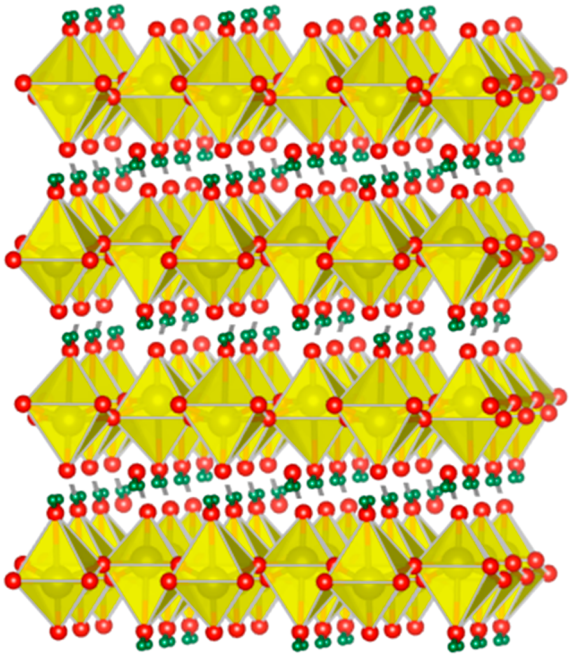

Figure 1. Crystal structure of tungsten trioxide hydrate, $WO_3{\cdot}H_2O$. Hydrogen atoms are illustrating in green, oxygen ions in red, and tungsten ions and also WO_6 octahedron in yellow color.

the atom and decomposed DOS including O(p), W(s), W(p), and W(d). The calculated band gap energy using GGA (Figure 2) is found to be direct with a value of 1.442 eV at the Γ point which is smaller than the experimental value (2.17 eV; Figure 7).[50] There are three groups that can be divided from the energy band including the following: (1) states lower than −2.1 eV below the Fermi level which originates from the overlap by the oxygen O(p) orbitals and the tungsten W(p) and W(d); (2) states between −2.1 and 0 eV which mainly form by the oxygen O(p) orbitals; and (3) bands above the Fermi level of predominantly tungsten W(d) character and overlapped by O(p) orbitals. Specifically, the deep-lying valence bands from 1.44 to 5.62 eV are due to the overlap by the oxygen O(p) orbitals and W(d) orbitals.

Figure 3 illustrates the band gap of $WO_3{\cdot}H_2O$ by using HSE06. It is found to be direct with a value of 2.318 eV at the Γ point, larger than the experimental values of 2.17 eV[50] and smaller than the estimated value of 2.5 eV for $WO_3{\cdot}H_2O$ spherical particle.[51,52] This result can be acceptable due to the exchange correlation (xc) functionals are needed to satisfy the agreement between the calculated and experimental band gaps of 2D-$WO_3.H_2O$ nanosheets. The study of the calculation of electron DOS for 2D-$WO_3{\cdot}H_2O$ nanosheets using the HSE06 method is shown on the right-hand side in Figure 3 with the atom and decomposed DOS including O(p), W(s), W(p), and W(d). The energy bands following the HSE06 method can be also classed into three groups: (1) states lower than −2.1 eV below the Fermi level, originating from the overlap by the oxygen O(p) orbitals and the tungsten W(p) and W(d); (2) states from −2.1 to 0 eV, mainly formed by the oxygen O(p) orbitals; and (3) bands above the Fermi level of predominantly tungsten W(d) character and overlapped by O(p) orbitals. It can be understood that the deep-lying valence bands between 2.318 and 7.221 eV are due to the overlapped by the O(p) orbitals and W(d) orbitals.

By DFT simulation, $WO_3{\cdot}H_2O$ has the estimated band gap around 2.17 eV that corresponds to the experimental value (Figure 7),[68] which was favorable not only for electrocatalyst but also for electrochemical capacitor. HSE06 method is appropriate functionals to understand the geometrical structure and electronic properties of 2D-$WO_3{\cdot}H_2O$.

2.2. Structure and Morphology Characterizations.

The crystal structure of the prepared sample 2D-$WO_3{\cdot}H_2O$ nanoflowers was identified by XRD measurement, which is shown in Figure 4. It can be seen that the XRD spectrum of 2D-$WO_3{\cdot}H_2O$ in Figure 4a shows the narrow peaks which reflect the good crystallinity and high-quality orthorhombic phase (JCPDS Card No. 43-0679).[51] The diffraction peaks of 2D-$WO_3{\cdot}H_2O$ corresponding to the hexagonal plane with the (020), (111), (040), (200), and (002) main planes at angles at around 16.3, 25.4, 33.2, 34, and 34.8°, which are associated with JCPDS Card No. 43-0679.[53−55] Raman spectra in Figure

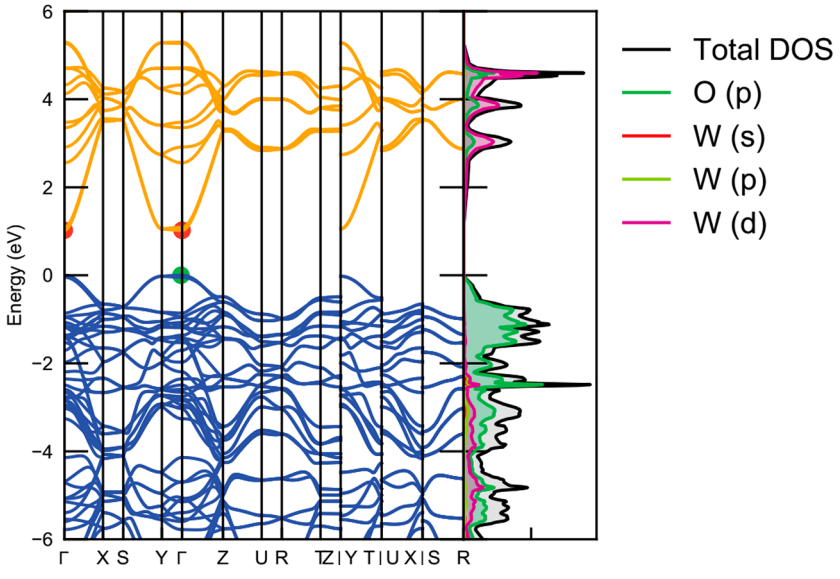

Figure 2. DOS and electronic energy band structures of $WO_3{\cdot}H_2O$ by using GGA method.

https://doi.org/10.1021/acsomega.1c06150
ACS Omega 2022, 7, 10115−10126

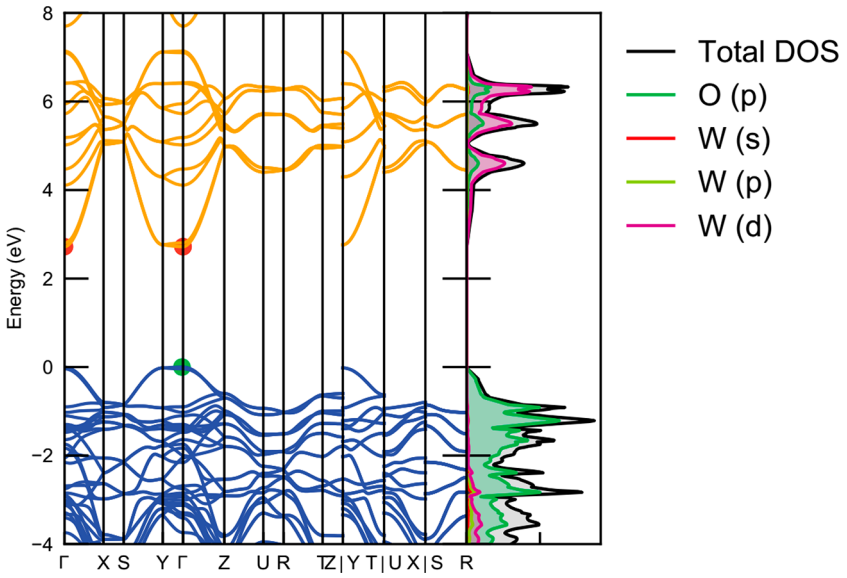

Figure 3. DOS and electronic energy band structures of $WO_3 \cdot H_2O$ by using HSE06 method.

4b show the crystalline of 2D-$WO_3 \cdot H_2O$ with two major characteristic potent and sharp peaks around 640 and 944 cm^{-1}, which illustrate the crystalline nature phase of metal oxide. The board peak located at 640 cm^{-1} corresponds to the stretching mode of the bridging ν(O−W−O) bond of the layer of the octahedral, sharing four equatorial oxygen atoms which suggest the exhibition of $WO_3 \cdot H_2O$ nanoplates thickness and hydration level.[55] The strong peak at around 944 cm^{-1} indicates the terminal bond of double-bond character belong to oxygen atom ν(W═O).[54] The N_2 adsorption−desorption isotherm (Figure 4c) and pore-size distribution (Figure 4d) were measured on the basis Brunauer−Emmett−Teller (BET) theory. From the Figure 4c, the specific surface area of 2D-$WO_3 \cdot H_2O$ with nanoflowers structure obtains a value of 2.3 $m^2 g^{-1}$, indicating a good 2D structure. The increase of the high relative pressure region of the N_2 isotherm in Figure 4c illustrates the existence of macropores. The large open hysteresis loop of P/P_0 from 0.45 to nearly 1 indicates the existence of mesopores in the samples.[56] Moreover, the plot of the N_2 isotherm at a low ratio of $P/P_0 < 0.45$ indicates the micropores.[57] In summary, the $WO_3 \cdot H_2O$ nanoflowers have a 2D plates structure containing micropores, macropores, and also mesopores. Figure 4d shows the pore-size distribution based on the Barrett−Joyner−Halenda analysis from N_2 adsorption−desorption isotherm. Herein, the distribution of pores via adsorption average pore with (4 V/A by BET) around 22.45 nm. The good BET results of 2D-$WO_3 \cdot H_2O$ with the large open hysteresis loop indicate the high surface active sites for fast redox reaction which serve perfectly for electrode materials for energy storage and conversion. Further, the X-ray photoelectron spectroscopy (XPS) for identifying the chemical states of 2D-$WO_3 \cdot H_2O$ nanoflowers was carried out and showed in Figure 4e,f. As seen in Figure 4e, the W 4f spectra show two major peaks at 35.2 and 37.4 eV which can be assigned to W $4f_{7/2}$ and W $4f_{5/2}$, respectively, for tungsten oxide which corresponds to the W^{6+} oxidation state of W.[58] The O 1s spectra in Figure 4f show two convoluted peaks at 531 and 532.7 eV are assigned to metal oxide (W−O) and hydroxide groups (-OH) which confirm the hydrated WO_3. The relatively high binding energy peak of the hydroxide group (-OH) corresponds to the hydrated phase in the material.

The morphology of 2D-$WO_3 \cdot H_2O$ nanoflowers sample was measured by scanning electron microscopy (SEM) and transmission electron microscopy (TEM), respectively. Panels a and b of Figure 5 show the SEM images of 2D-$WO_3 \cdot H_2O$ at different magnification. The thin nanoplates were found with the highly uniform size and square shape, which gather into a flower morphology. Panels c−e of Figure 5 illustrate clearly the TEM image of stacked 2D-$WO_3 \cdot H_2O$ in according with the SEM images. At high-resolution TEM (HRTEM) in Figure 6a−c, the 2D-$WO_3 \cdot H_2O$ nanoplates show the lattice spacing approximately 0.27 nm, which corresponds to (021) plane. Moreover, the TEM mapping of 2D-$WO_3 \cdot H_2O$ confirms the stacked nanoplate with the attribution of tungsten and oxygen elements (Figure 6c−f).

The UV−vis absorption spectroscopy in Figure 7a shows the optical respone of 2D-$WO_3 \cdot H_2O$ in the UV region. The Tauc optical band gap (E_g) value of 2D-$WO_3 \cdot H_2O$ nanoflowers were calculated from the absorption plots and given in equation:[68] $(\alpha h\nu)^2 = B(h\nu - E_g)$, where $h\nu$ is the energy of the incident photon and B is an energy-independent constant. E_g was found to be 2.17 eV (Figure 7b) on the basis of the Tauc plot and the UV absorption spectra.

2.3. Electrochemical Studies. Electrocatalytic HER measurements were studied by using glassy carbon electrode modified with 2D-$WO_3 \cdot H_2O$ nanoflowers in 0.5 M H_2SO_4 electrolyte. Herein, the working principle of water electrolysis of metal catalyst in acidic electrolyte can be explained by the following reaction: the cathodic half-cell reaction of hydrogen evolution reaction ($2H^+ + 2\ e^- \rightarrow H_2$), the anodic half-cell reaction of hydrogen oxidation reaction (HOR) ($H_2O \rightarrow 2H^+ + \frac{1}{2}O_2 + 2e^-$), and the full cell reaction ($H_2O \rightarrow H_2 + \frac{1}{2}O_2$).

Figure 8a show the representative linear sweep voltammetry (LSV) plots of 2D-$WO_3 \cdot H_2O$ in comparison with bare glassy carbon electrode, and Pt/C at 5 mV s^{-1} in the voltage window of 0−0.8 V vs RHE. All measurements were converted into RHE with Ag/AgCl reference electrode. As can be seen in Figure 7a, the Pt/C shows a best overpotential value of 86 mV at current density of −10 mA cm^{-2}, which is known as the best material for electrocatalytic HER. The 2D-$WO_3 \cdot H_2O$ exhibits amazing low overpotential value of 290 mV at initial time and

https://doi.org/10.1021/acsomega.1c06150
ACS Omega 2022, 7, 10115−10126

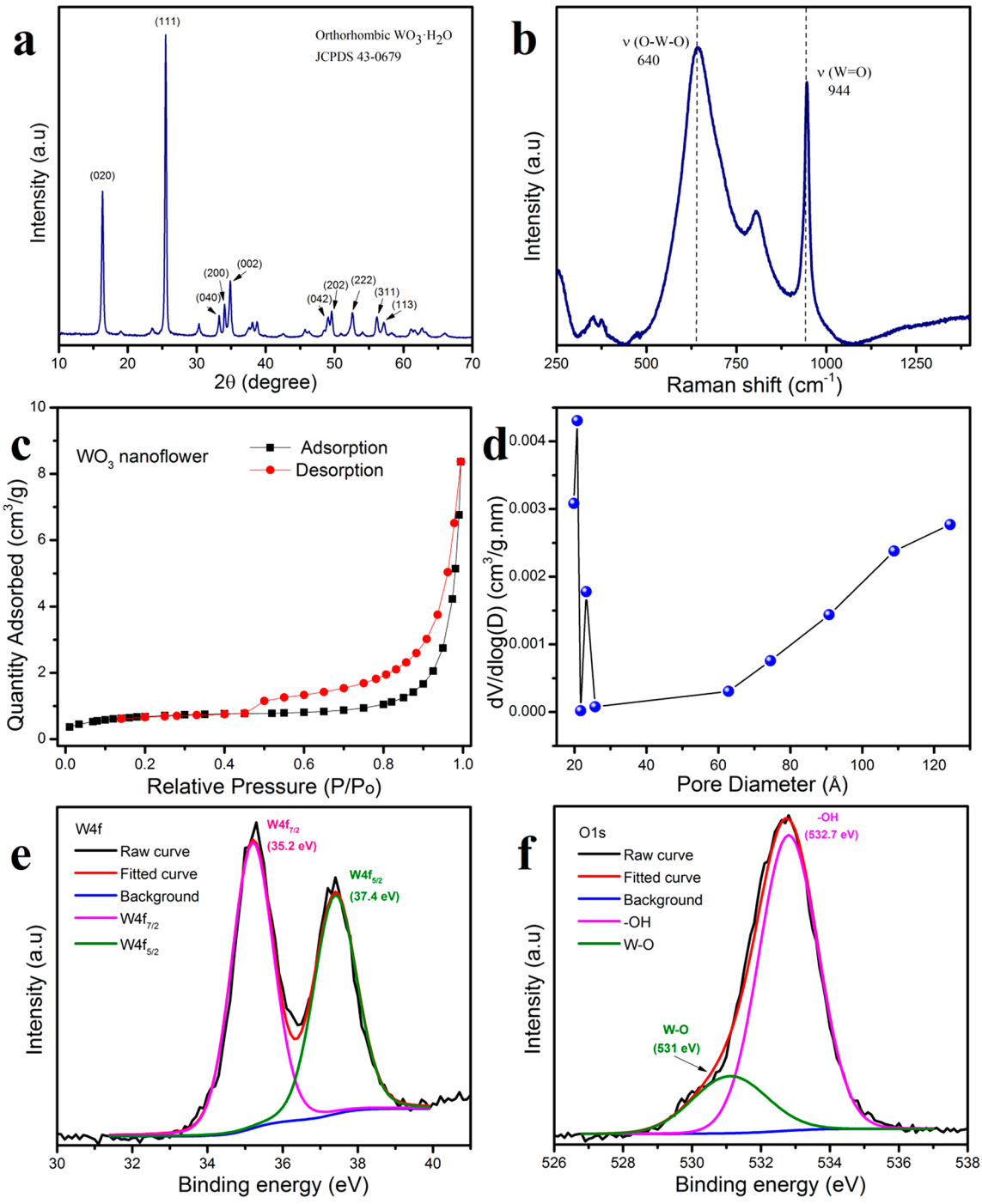

Figure 4. (a) XRD pattern, (b) Raman spectra, (c) nitrogen adsorption/desorption, (d) pore-size distribution, and (e, f) XPS spectra of W 4f and O 1s of $WO_3 \cdot H_2O$ nanoflowers.

310 mV after stability over 30 h at the same current density of −10 mA cm^{-2}, indicating excellent strongly electrochemical durability. Figure 8b reveals that the Tafel slope following eq 1 of 2D-$WO_3 \cdot H_2O$ was 131 mV dec^{-1} at the initial time and 138 mV dec^{-1} after 30 h, respectively, indicating a good Volmer–Heyrovsky mechanism for the HER. For further study of the transport kinetic of 2D-$WO_3 \cdot H_2O$, the electrochemical impedance spectroscopy (EIS) spectra were recorded and depicted in Figure 8c with the inset figure of equivalent circuit model (Randles circuit). The equivalent series resistance of 2D-$WO_3 \cdot H_2O$ show solution resistance (R_S) around 40 Ω and charge transfer resistance (R_{CT}) of approximately 140 Ω. The low equivalent series resistance of 2D-$WO_3 \cdot H_2O$ indicates good electrical conductivity. The stability of catalyst over the long-term operation over 30 h at overpotential of 290 mV vs RHE investigates the good catalyst durability of 2D-$WO_3 \cdot H_2O$, which indicates the suitability of 2D-$WO_3 \cdot H_2O$ a catalyst for the HER.

Further, the 2D-$WO_3 \cdot H_2O$ nanoflowers material was investigated as a promising material for electrochemical capacitor (or supercapacitor). The three electrode system for 2D-$WO_3 \cdot H_2O$ nanoflowers working electrode in 1 M Na_2SO_4 aqueous electrolyte was investigated by cyclic voltammetry, electrochemical impedance spectroscopy, and galvanostatic

https://doi.org/10.1021/acsomega.1c06150
ACS Omega 2022, 7, 10115−10126

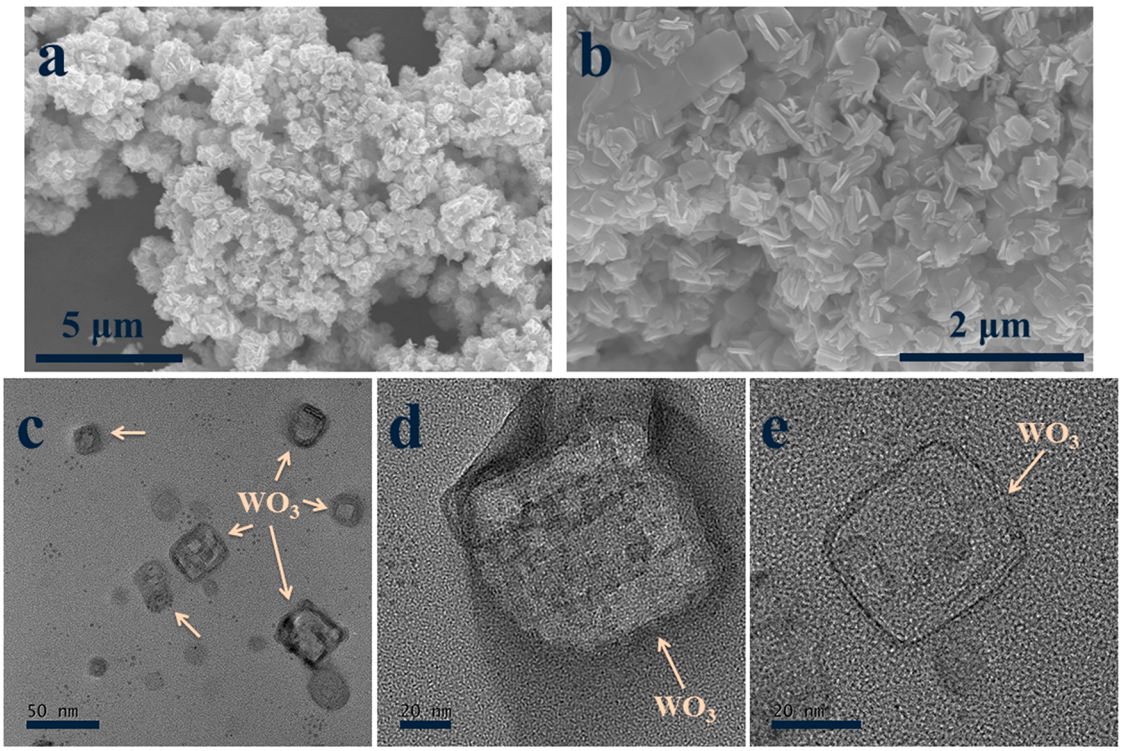

Figure 5. (a, b) SEM and (c−e) TEM images of $WO_3 \cdot H_2O$ nanoflowers.

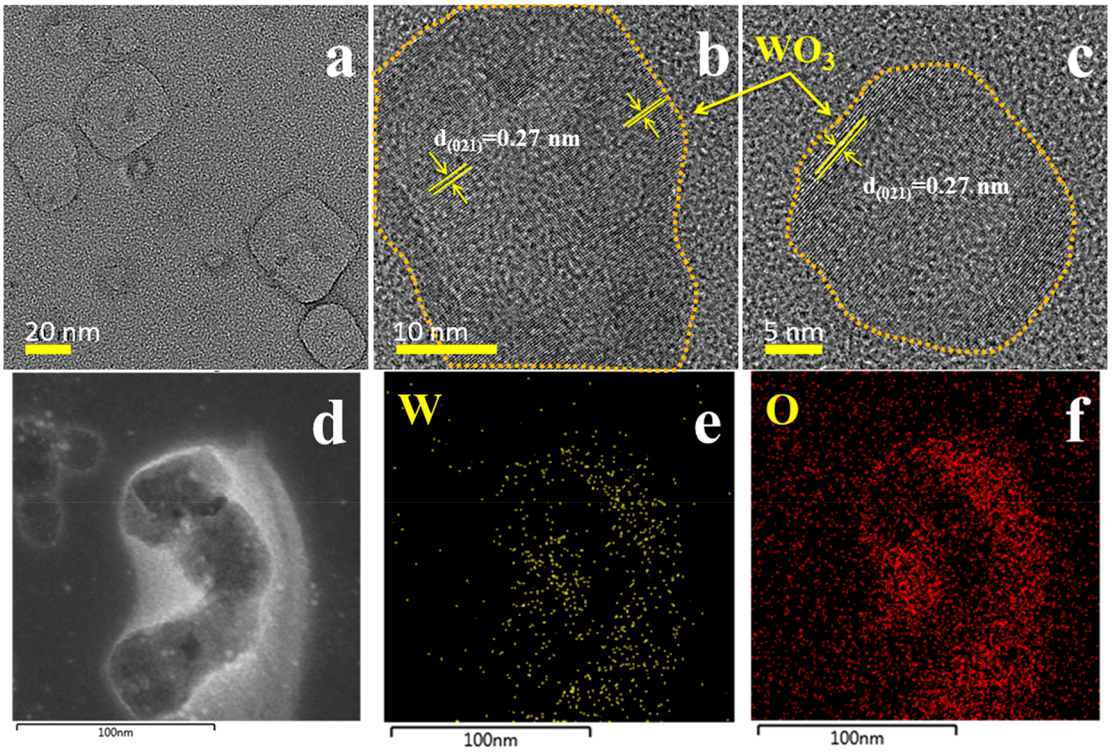

Figure 6. (a−c) HRTEM and (d−f) relative mapping elements of $WO_3 \cdot H_2O$ nanoflowers.

charge−discharge (GCD) measurements. As shown in Figure 9a, the CV curves at various scan rates in the range of [10−120 mV cm^{-1}], which exhibit a nonrectangular shape with Faradaic humps, indicating the combination between double layer capacitive and pseudocapacitive behavior.[59,60] At various different current densities from low to high, the shape of the CV curves increase linearity, indicating the excellent behavior rate performance. Further measurement of GCD at different current densities was studied and shown in Figure 9b.

The GCD curves have nonsymmetrical shape and almost no voltage drop which indicate the good capacitive behavior and contribute pseudocapacitive behavior and good Coulombic efficiency. As calculated from the GCD curves, the maximum specific capacitance obtain a value of 71.25 F g^{-1} at current

https://doi.org/10.1021/acsomega.1c06150
ACS Omega 2022, 7, 10115−10126

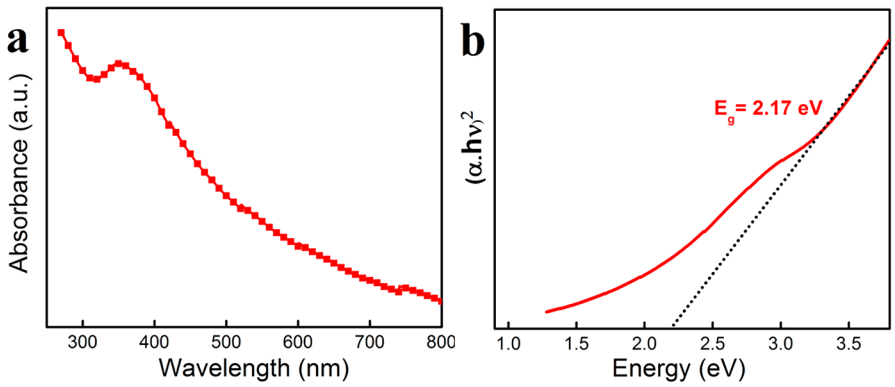

Figure 7. (a) UV−vis spectra and (b) related band gap from UV−vis of 2D-WO_3·H_2O.

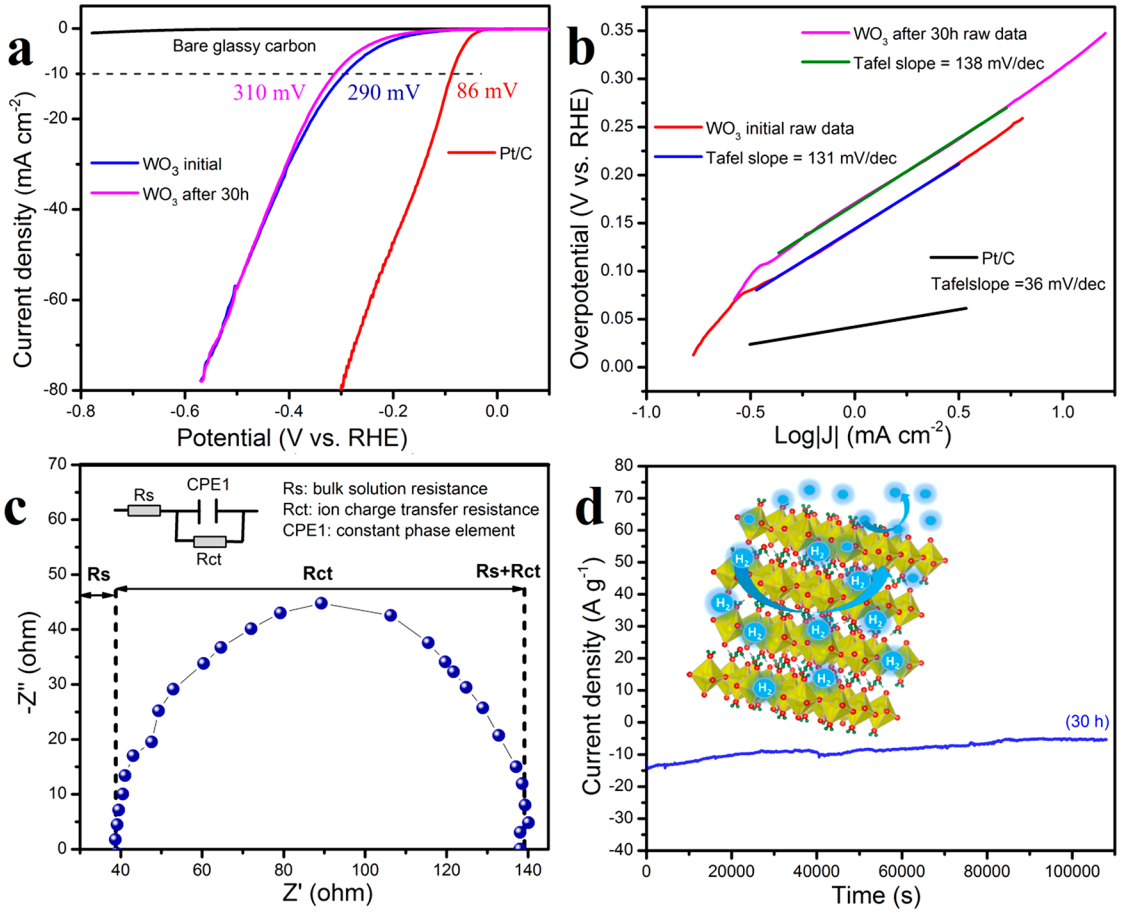

Figure 8. Electrochemical catalyst of hydrogen evolution reaction: (a) LSV plots, (b) Tafel plots, (c) EIS plot, and (d) *i*−*t* plot of WO_3·H_2O nanoflowers.

density of 2 A g^{-1} with good Coulombic efficiency approximately of 98.2%. Figure 9c shows the specific capacitance under high current densities from 8 to 2 A g^{-1}. On the basis of eq 2, at high current density of *c*, the specific capacitance still obtains a value of 25 F g^{-1} with excellent Coulombic efficiency of 100% (eq 5). The 2D-WO_3 working electrode obtains the maximum specific capacitance of 71.25 F g^{-1} at 2 A g^{-1}. The slight decrease of Coulombic efficiency from high to low current density maybe come from the strong Faradaic reaction at interface layer of electrode/electrolyte at low applied current. Electrochemical impedance spectroscopy is one of the critical techniques of electrochemical studies. As the Nyquist plot of 2D-WO_3·H_2O in inset Figure 9c, the small semicircle at high frequency illustrates the charge transfer resistance while the straight line at low frequency indicates the ion diffusion from the electrolyte to the electrode layer.[60] Typically, the equivalent resistance of the Nyquist plot obtains a low value of 19.6 Ω which indicates the good electrical conductivity of electrode material: 2D-WO_3·H_2O. Herein, the equivalent series resistance is the combination of electrode resistance, resistance of electrolyte, and resistance of electrode/electrolyte interface.[61] Figure 9d demonstrates the relationship between the energy density and power density (Ragone plot). From eqs 3 and 4, the maximum energy density of 2D-WO_3·

https://doi.org/10.1021/acsomega.1c06150
ACS Omega 2022, 7, 10115−10126

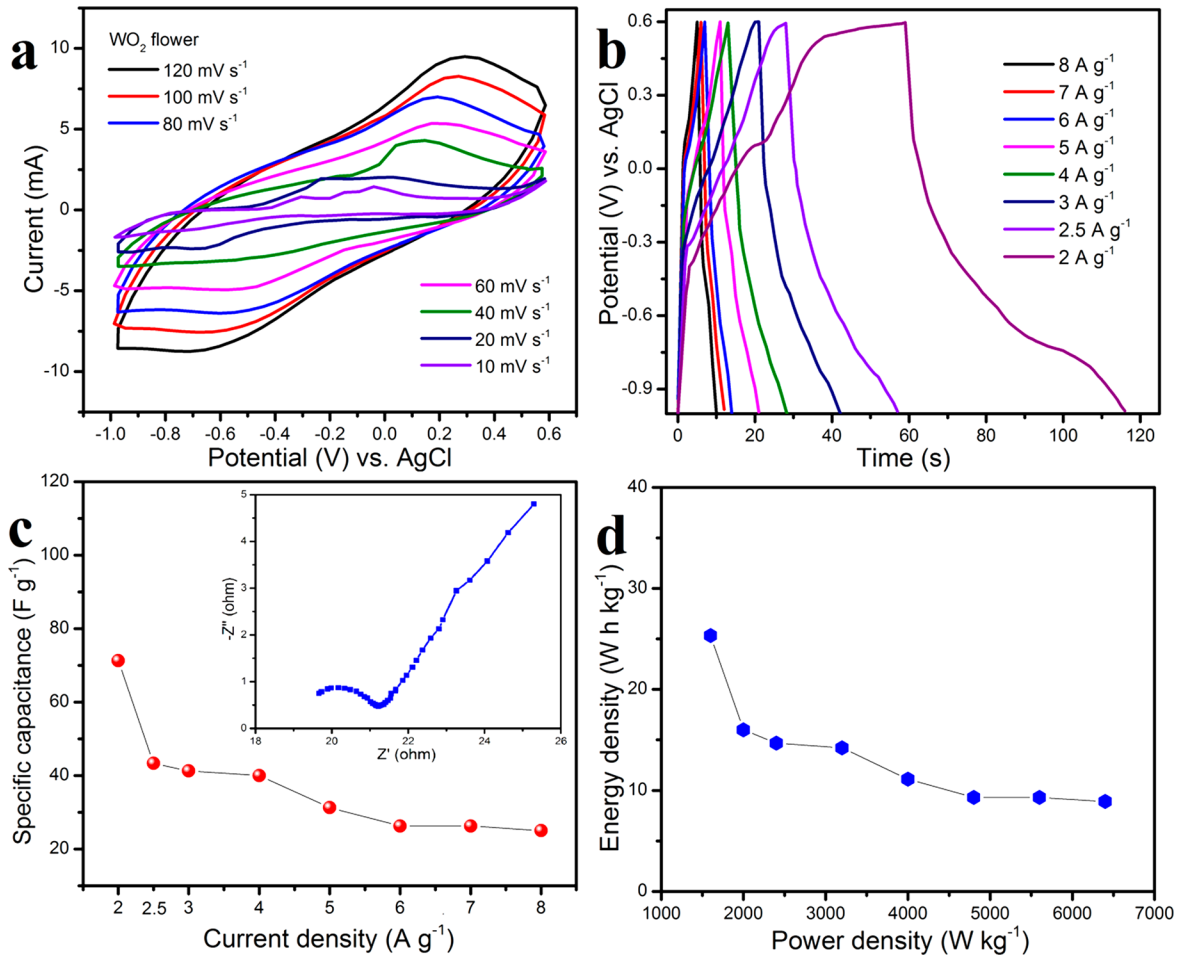

Figure 9. Electrochemical plots of three electrode system for supercapacitor studies of $WO_3·H_2O$ nanoflowers: (a) CV curves, (b) GCD curves, (c) specific capacitance at various current densities, and (d) Ragone plot.

Table 2. Summary of Synthesis of WO_3 Material and Potential Applications in Energy Storage and Conversion

precursor	solvent	method	phase	corresponding performance for catalyst and energy storage	ref
WCl_6	ethanol	wet chemical	$WO_3·H_2O$ nanoplates	hydrogen generation rates of 1.1 (mmol/cm^2)/h	51
$Na_2WO_4·2H_2O$	H_2O with HCl diluted solution	hydrothermal	$WO_3·H_2O$ spherical particles	performance of photodegradation delivery the value of k = 0.0244 min^{-1}	52
$Na_2WO_4·2H_2O$ graphene oxide, and oxalic acid	H_2O	hydrothermal	$WO_3·H_2O$/rGO flower-like hierarchical	supercapcitor with 244 F/g at 1 A g^{-1}	53
Na_2WO_4 and NaCl	H_2O	hydrothermal	anhydrous WO_3nanorods	hydrogen evolution reaction of WO_3 with overpotential of 89 mV and Tafel slope of 55 mV dec^{-1}	58
$Na_2WO_4·2H_2ONa_2SO_4$, oxalic acid	H_2O	hydrothermal	anhydrous WO_3nanorods	WO_3 nanorods presenting 93% of MB photodegradation, and electrochemical capcitor with 919.26 F g^{-1} at 0.7 A g^{-1}	62
$Na_2WO_4·2H_2OHCl$	H_2O	wet chemical	$WO_3·H_2O$ sheets like nanoflowers	low overpotential value of 290 mV at initial time and 310 mV after stability over 30 h; electrochemical capacitance of 71.25 F g^{-1} at high current density of 2 A g^{-1}	this work

H_2O working electrode exhibits a value of 25.33 W h kg^{-1} at power density of 1600 W kg^{-1}. As a highest power density of 6400 W kg^{-1}, the 2D-$WO_3·H_2O$ still obtained a good value of 8.9 W h kg^{-1}. The excellent electrochemical results of 2D-$WO_3·H_2O$ are based on the three electrode system, making it a promising candidate for the hydrogen evolution reaction and electrochemical capacitor applications (Table 2). The hydrated WO_3 with two-dimensional structures in this report provides another perspective on the WO_3 material to diversify the studies on this interesting material, besides the previous research on anhydrous WO_3.[62−67] Figure 10 illustrates an energy diagram of 2D-$WO_3·H_2O$ (Figure 10a) and our future goal for fabrication complex devices which incorporate electrochemical capacitor and catalyst (Figure 10b).

3. CONCLUSIONS

In conclusion, we demonstrate 2D-$WO_3·H_2O$ nanoflowers for electrochemical studies of energy conversion and storage applications. The high conductivity and two-dimensional structure of the WO_3 material enables high efficiency of exposed active sites for catalyst. Moreover, 2D-$WO_3·H_2O$ nanoflowers electrode layers provide a large surface area for ion

https://doi.org/10.1021/acsomega.1c06150
ACS Omega 2022, 7, 10115−10126

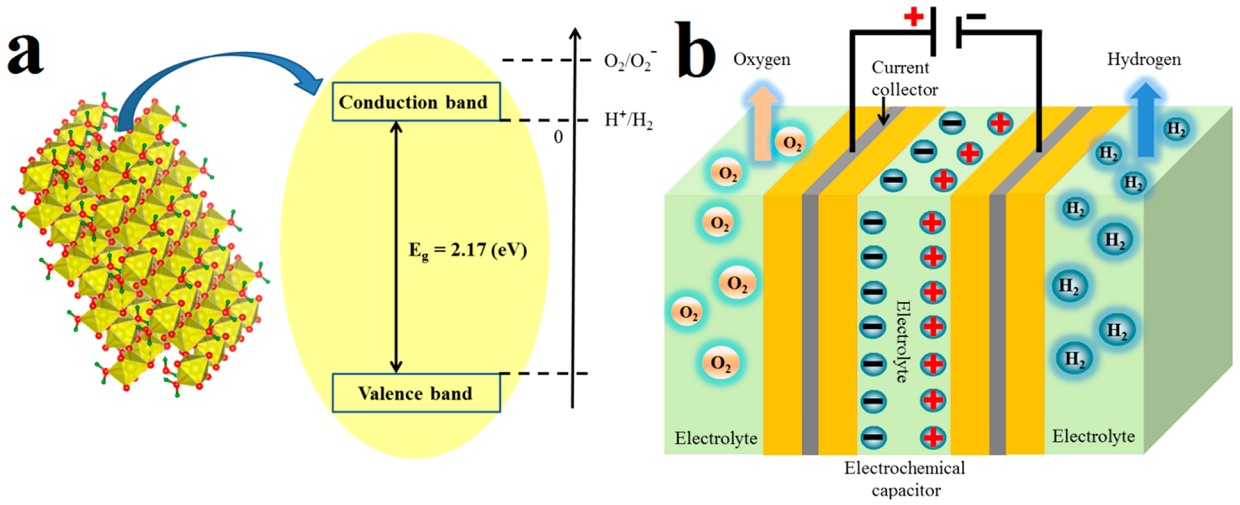

Figure 10. (a) Energy diagram of 2D-$WO_3{\cdot}H_2O$ and (b) proposed device for both HER and supercapacitor.

transport during charge−discharge process to enhance the electrochemical behavior of supercapacitor. All of the above metrics make 2D-$WO_3{\cdot}H_2O$ nanoflowers attractive as a promising material for electrochemical studies for hydrogen evolution reaction and supercapacitor.

4. EXPERIMENTAL SECTION

4.1. Materials. $Na_2WO_4{\cdot}2H_2O$, oxalic acid ($H_2C_2O_4$), poly(vinylidene fluoride) (PVDF) with MW 534,000 by GPC, and aqueous electrolyte−standard 0.5 M H_2SO_4 solution for HER measurement were purchased from Sigma−Aldrich. 1-Methyl-2-pyrrolidinone (C_5H_9NO), dimethylformamide [$(CH_3)_2NC(O)H$, DMF], and Na_2SO_4 were ordered from Alfa Aesar. The ultrapure water was prepared by Milipore Mili-Q UF system at room temperature with resistivity of 18.2 MΩ cm.

4.2. Preparation of $WO_3.H_2O$ Nanoflowers. First, 50 mL of 0.2 M Na_2WO_4 was prepared by dissolving $Na_2WO_4{\cdot}2H_2O$ in DI water with constant stirring to obtain a transparent solution. Then, 50 mL of 2 M HCl was dropped slowly and constantly by a 100 mL buret into the above solution with constant stirring until a yellow precipitation was obtained. Second, a certain amount of oxalic acid was added slowly into the above solution and held stable in 3 h at 90 °C. After reaction, the final yellow precipitate was collected after centrifugation and washing with DI water, ethanol, and followed by drying at 100 °C in a vacuum oven in 8 h to obtain $WO_3{\cdot}H_2O$ nanoflowers.

4.3. $WO_3.H_2O$ Characterization. The structures of the $WO_3{\cdot}H_2O$ nanoflowers was carried out by using scanning electron microscopy (FE-SEM) from Hitachi SU8000 with the high accelerating voltage of 15 kV, transmission electron microscopy from JEM-2100F with 200 kV field emission. The morphologies of $WO_3.H_2O$ nanoflowers were studied by Raman spectroscopy from Jobin Yvon-Horiba (the samples were carried out by using the 520 nm line of an argon laser), X-ray diffractometry (XRD; D2 Bruker; Cu Kα tube), X-ray photoelectron spectroscopy (XPS; Escalab 250Xi, Thermo Scientific). The specific surface area and pore-size distribution of 2D-WO_3 nanoflowers was carried out by porosity analyzer (Micromeritics, ASAP 2020).

4.4. Electrochemical Catalyst. In the preparation of $WO_3{\cdot}H_2O$ for hydrogen evolution reaction, the catalyst ink was prepared by solution casting method: 3 mg of WO_3 and 1 mL of DMF were mixed together with ultrasonic in 30 min. Then, $WO_3{\cdot}H_2O$ ink (5 μL) was dropped onto glassy carbon electrode (3 mm in diameter) and kept naturally in hood for drying. Finally, 5 μL of 20% Nafion was covered on the glassy carbon electrode-modified with 2D-$WO_3{\cdot}H_2O$.

The electrochemical studies consisting cyclic voltammetry, linear sweep voltammetry, and electrochemical impedance spectroscopy were characterized by three electrode system using Zahner Zenium electrochemical workstation (Z 2.23, Germany), where a graphite rode as counter electrode, a Ag/AgCl as reference electrode, glassy carbon electrode-modified with 2D-$WO_3{\cdot}H_2O$ as working electrode, and standard commercial solution 0.5 M H_2SO_4 acidic electrolyte. Herein, the LSV plots were measured at a scan rate of 5 mV s^{-1} in a range from 0 to −0.8 V vs reversible hydrogen electrode (RHE). The stability measurements of the 2D-$WO_3{\cdot}H_2O$ material for HER studies were tested by measuring $i-t$ curves over 30 h at an overpotential values. The electrochemical potential was calibrated with reversible hydrogen electrodeby equation: $E_{RHE} = E_{SCE} + 0.209 + 0.0591pH = 0.23$. From LSV plots, we can calculate the Tafel plots which correspond to the inherent properties of the catalysts by using the Tafel equation:[41]

$$\eta = b \log j + a \quad (1)$$

where η, b, j, and a are the overpotential, Tafel slope, current density, and a constant, respectively.

4.5. Electrochemical Capacitor. The $WO_3{\cdot}H_2O$ supercapacitor electrode for three electrode system was prepared following solution casting method. The working electrodes were prepared by solution casting method; 9 mg of $WO_3{\cdot}H_2O$ (90%) and 1 mg of PVDF (10%) were mixed together in 0.2 mL of NMP solvent with constant stirring at 60 °C in 12 h to obtain a uniform dark yellow slurry. Then, 20 μL of this dark yellow slurry was coated onto carbon paper substrate (1 × 1 cm^2) and dried at 80 °C in 2 days to obtain $WO_3{\cdot}H_2O$ working electrode (1 mg cm^{-2}).

The electrochemical studies of electrochemical capacitors based on cyclic voltammetry, electrochemical impedance spectroscopy, and galvanostatic charge−discharge were measured in three electrode system by using Zahner Zenium (version Z 2.23 from Germany) electrochemical workstation

https://doi.org/10.1021/acsomega.1c06150
ACS Omega 2022, 7, 10115−10126

with $WO_3 \cdot H_2O$ working electrode, Ag/AgCl reference electrode, and platinum plate (2×6 cm^2) counter electrode. From the charge−discharge curves, the specific capacitances of the supercapacitor electrode (C, F g^{-1}) can be calculated by using the following equations:[42,43]

$$C = \frac{I\Delta t}{\Delta V m_{ac}} \quad (2)$$

The energy density (E, W h kg^{-1}) at various power density (P, W kg^{-1}) values can be estimated by using the following equations:[42,43]

$$E = \frac{C(\Delta V)^2}{2} \times \frac{1000}{3600} \quad (3)$$

$$P = \frac{E \times 3600}{\Delta t} \quad (4)$$

where I (A) is the discharge current, Δt is the discharge time, ΔV is the potential voltage, and m_{ac} is the weight of the active materials on working electrode (including binder).

The Coulombic efficiency can calculate from GCD curves by following equation:

$$\varepsilon = t_{dc}/t_c \times 100\% \quad (5)$$

where t_{dc} is the discharge time and t_c is the charge time.

AUTHOR INFORMATION

Corresponding Authors

Phuoc Anh Le − *Institute of Sustainability Science, VNU Vietnam Japan University, Vietnam National University, Hanoi 100000, Vietnam*; Email: lephuocanh86@vnu.edu.vn

Thi Viet Bac Phung − *Institute of Sustainability Science, VNU Vietnam Japan University, Vietnam National University, Hanoi 100000, Vietnam*; orcid.org/0000-0001-7717-2538; Email: ptv.bac@vju.ac.vn

Authors

Van Qui Le − *Department of Materials Science and Engineering, National Yang Ming Chiao Tung University, Hsinchu 300093, Taiwan*

Thien Lan Tran − *Institute of Sustainability Science, VNU Vietnam Japan University, Vietnam National University, Hanoi 100000, Vietnam; Department of Physics, Hue University of Education, Hue University, Hue 530000, Vietnam*

Nghia Trong Nguyen − *School of Chemical Engineering, Hanoi University of Science and Technology, Hanoi 100000, Vietnam*

Complete contact information is available at: https://pubs.acs.org/10.1021/acsomega.1c06150

Notes

The authors declare no competing financial interest.

ACKNOWLEDGMENTS

This research is funded by Vietnam National University, Hanoi (VNU) under Project No. QG.20.62. We acknowledge the facility support from the JICA Technical Cooperation 2 (TC2) project in VNU Vietnam−Japan University under Research Project VJU.JICA.21.01.

REFERENCES

(1) Lei, Z.; Lee, J. M.; Singh, G.; Sathish, C. I.; Chu, X.; Al-Muhtaseb, A. H.; Vinu, A.; Yi, J. Recent advances of layered-transition metal oxides for energy-related applications. *Energy Storage Mater.* **2021**, *36*, 514−550.

(2) Fang, S.; Bresser, D.; Passerini, S. Transition Metal Oxide Anodes for Electrochemical Energy Storage in Lithium- and Sodium-Ion Batteries. *Adv. Energy Mater.* **2020**, *10*, 1902485.

(3) Mohd Abdah, M. A. A.; Azman, N. H. N.; Kulandaivalu, S.; Sulaiman, Y. Review of the use of transition-metal-oxide and conducting polymer-based fibres for high-performance supercapacitors. *Mater. Des* **2020**, *186*, 108199.

(4) An, C.; Zhang, Y.; Guo, H.; Wang, Y. Metal oxide-based supercapacitors: progress and prospectives. *Nanoscale Adv.* **2019**, *1*, 4644−4658.

(5) Lu, X.; Wang, C.; Favier, F.; Pinna, N. Electrospun Nanomaterials for Supercapacitor Electrodes: Designed Architectures and Electrochemical Performance. *Adv. Energy Mater.* **2017**, *7*, 1601301.

(6) Raj, S.; Kar, P.; Roy, P. Facile synthesis of flower-like morphology $Cu_{0.27}Co_{2.73}O_4$ for a high-performance supercapattery with extraordinary cycling stability. *Chem. Commun.* **2018**, *54*, 12400−12403.

(7) Shabangoli, Y.; Rahmanifar, M. S.; El-Kady, M. F. E.; Noori, A.; Mousavi, M. F.; Kaner, R. B. Thionine functionalized 3D graphene aerogel: Combining simplicity and efficiency in fabrication of a metal-free redox supercapacitor. *Adv. Energy Mater.* **2018**, *8*, 1802869.

(8) Li, Y.; Yu, Z. G.; Wang, L.; Weng, Y.; Tang, C. S.; Yin, X.; Han, K.; Wu, H.; Yu, X.; Wong, L. M.; Wan, D.; Wang, X. R.; Chai, J.; Zhang, Y. W.; Wang, S.; Wang, J.; Wee, A. T. S.; Breese, M. B. H.; Pennycook, S. J.; Venkatesan, T.; Dong, S.; Xue, J. M.; Chen, J. Electronic-reconstruction-enhanced hydrogen evolution catalysis in oxide polymorphs. *Nat. Commun.* **2019**, *10*, 3149.

(9) Wen, P.; Wang, C.; Lan, Y.; Jiang, X.; Ren, L. *In situ* synthesis of crystalline Ag−WO_3 nanosheets with enhanced solar photo-electrochemical performance for splitting water. *CrystEngComm* **2020**, *22*, 105−112.

(10) Jiang, P.; Yang, Y.; Shi, R.; Xia, G.; Chen, J.; Su, J.; Chen, Q. Pt-like electrocatalytic behavior of Ru−MoO_2 nanocomposites for the hydrogen evolution reaction. *J. Mater. Chem. A* **2017**, *5*, 5475−5485.

(11) Santato, C.; Odziemkowski, M.; Ulmann, M.; Augustynski, J. Crystallographically Oriented Mesoporous WO_3 Films: Synthesis, Characterization, and Applications. *J. Am. Chem. Soc.* **2001**, *123*, 10639−10649.

(12) Tan, H. T.; Sun, W.; Wang, L.; Yan, Q. 2D transition metal oxides/hydroxides for energy-storage applications. *ChemNanoMat* **2016**, *2* (7), 562−577.

(13) Mei, J.; Liao, T.; Kou, L.; Sun, Z. Two-dimensional metal oxide nanomaterials for next-generation rechargeable batteries. *Adv. Mater.* **2017**, *29* (48), 1700176.

(14) Yuan, W.; Huang, Q.; Yang, X.; Cui, Z.; Zhu, S.; Li, Z.; Du, S.; Qiu, N.; Liang, Y. Two-Dimensional Lamellar Mo_2C for Electrochemical Hydrogen Production: Insights into the Origin of Hydrogen Evolution Reaction Activity in Acidic and Alkaline Electrolytes. *ACS Appl. Mater. Interfaces* **2018**, *10*, 40500−40508.

(15) Wang, D.; Astruc, D. The recent development of efficient Earth-abundant transition-metal nanocatalysts. *Chem. Soc. Rev.* **2017**, *46*, 816−854.

(16) Chen, Y.; Yang, K.; Jiang, B.; Li, J.; Zeng, M.; Fu, L. Emerging two-dimensional nanomaterials for electrochemical hydrogen evolution. *J. Mater. Chem. A* **2017**, *5*, 8187−8208.

(17) Chandrasekaran, S.; Yao, L.; Deng, L.; Bowen, C.; Zhang, Y.; Chen, S.; Lin, Z.; Peng, F.; Zhang, P. Recent advances in metal sulfides: from controlled fabrication to electrocatalytic, photocatalytic and photoelectrochemical water splitting and beyond. *Chem. Soc. Rev.* **2019**, *48*, 4178−4280.

(18) Jiao, S.; Fu, X.; Wang, S.; Zhao, Y. Perfecting electrocatalysts via imperfections: towards the large-scale deployment of water electrolysis technology. *Energy Environ. Sci.* **2021**, *14*, 1722−1770.

https://doi.org/10.1021/acsomega.1c06150
ACS Omega 2022, 7, 10115−10126

(19) Wang, T.; Zhang, X.; Yang, P.; Jiang, S. P. Vertically aligned MoS_2 nanosheets on N-doped carbon nanotubes with NiFe alloy for overall water splitting. *Inorg. Chem. Front* **2020**, *7*, 3578−3587.
(20) Zou, X.; Zhang, Y. Noble metal-free hydrogen evolution catalysts for water splitting. *Chem. Soc. Rev.* **2015**, *44*, 5148−5180.
(21) Chen, L.; Shi, J. Chemical-assisted hydrogen electrocatalytic evolution reaction (CAHER). *J. Mater. Chem. A* **2018**, *6*, 13538−13548.
(22) Xu, H.; Ye, K.; Zhu, K.; Yin, Y.; Yan, J.; Wang, G.; Cao, D. Template-directed assembly of urchin-like CoSx/Co-MOF as an efficient bifunctional electrocatalyst for overall water and urea electrolysis. *Inorg. Chem. Front* **2020**, *7*, 2602−2610.
(23) Zheng, Y.; Jiao, Y.; Jaroniec, M.; Qiao, S. Advancing the electrochemistry of the hydrogen evolution reaction through combining experiment and theory. *Angew. Chem., Int. Ed* **2015**, *54*, 52−65.
(24) Sarkar, S.; Peter, S. C. An overview on Pd-based electrocatalysts for the hydrogen evolution reaction. *Inorg. Chem. Front* **2018**, *5*, 2060−2080.
(25) Huang, X.; Wang, X.; Jiang, P.; Lan, K.; Qin, J.; Gong, L.; Wang, K.; Yang, M.; Ma, L.; Li, R. Ultrasmall MoP encapsulated in nitrogen-doped carbon hybrid frameworks for highly efficient hydrogen evolution reaction in both acid and alkaline solutions. *Inorg. Chem. Front.* **2019**, *6*, 1482−1489.
(26) Tong, R.; Ng, K. W.; Wang, X.; Wang, S.; Wang, X.; Pan, H. Two-dimensional materials as novel co-catalysts for efficient solar-driven hydrogen production. *J. Mater. Chem. A* **2020**, *8*, 23202−23230.
(27) Pei, Y.; Cheng, Y.; Chen, J.; Smith, W.; Dong, P.; Ajayan, P. M.; Ye, M.; Shen, J. Recent developments of transition metal phosphides as catalysts in the energy conversion field. *J. Mater. Chem. A* **2018**, *6*, 23220−23243.
(28) Han, N.; Liu, P.; Jiang, J.; Ai, L.; Shao, Z.; Liu, S. Recent advances in nanostructured metal nitrides for water splitting. *J. Mater. Chem. A* **2018**, *6*, 19912−19933.
(29) Yan, Y.; Xia, B.; Xu, Z.; Wang, X. Recent Development of Molybdenum Sulfides as Advanced Electrocatalysts for Hydrogen Evolution Reaction. *ACS Catal.* **2014**, *4*, 1693−1705.
(30) Zhu, Y.; Lin, Q.; Zhong, Y.; Tahini, H. A.; Shao, Z.; Wang, H. Metal oxide-based materials as an emerging family of hydrogen evolution electrocatalysts. *Energy Environ. Sci.* **2020**, *13*, 3361−3392.
(31) Feng, H.; Xu, Z.; Ren, L.; Liu, C.; Zhuang, J.; Hu, Z.; Xu, X.; Chen, J.; Wang, J.; Hao, W.; Du, Y.; Dou, S. X. Activating Titania for Efficient Electrocatalysis by Vacancy Engineering. *ACS Catal.* **2018**, *8* (5), 4288−4293.
(32) Datta, R. S.; Haque, F.; Mohiuddin, M.; Carey, B. J.; Syed, N.; Zavabeti, A.; Zhang, B.; Khan, H.; Berean, K. J.; Ou, J. Z.; Mahmood, N.; Daeneke, T.; Kalantar-zadeh, K. Highly active two dimensional α-MoO_{3-x} for the electrocatalytic hydrogen evolution reaction. *J. Mater. Chem. A* **2017**, *5*, 24223−24231.
(33) Zhao, Y.; Chang, C.; Teng, F.; Zhao, Y.; Chen, G.; Shi, R.; Waterhouse, G. I. N.; Huang, W.; Zhang, T. Water Splitting: Defect-Engineered Ultrathin δ-MnO2 Nanosheet Arrays as Bifunctional Electrodes for Efficient Overall Water Splitting. *Adv. Energy Mater.* **2017**, *7*, 1700005.
(34) Li, Y.; Yu, Z. G.; Wang, L.; Weng, Y.; Tang, C. S.; Yin, X.; Han, K.; Wu, H.; Yu, X.; Wong, L. M.; Wan, D.; Wang, W. R.; Chai, J.; Zhang, Y. W.; Wang, S.; Wang, J.; Wee, A. T. S.; Breese, M. B. H.; Pennycook, S. T.; Venkatesan, T.; Dong, S.; Xue, J. M.; Chen, J. Electronic-reconstruction-enhanced hydrogen evolution catalysis in oxide polymorphs. *Nat. Commun.* **2019**, *10*, 3149.
(35) Zheng, M.; Xiao, Z.; Li, L.; Gu, P.; Dai, X.; Tang, H.; Hu, Q.; Xue, H.; Pang, H. Hierarchically nanostructured transition metal oxides for supercapacitors. *Sci. China Mater.* **2018**, *61* (2), 185−209.
(36) Zhong, Y.; Xia, X.; Shi, F.; Zhan, J.; Tu, J.; Fan, H. J. Transition Metal Carbides and Nitrides in Energy Storage and Conversion. *Adv. Sci.* **2016**, *3*, 1500286.
(37) Quispe-Garrido, V.; Cerron-Calle, G. A.; Bazan-Aguilar, A.; Ruiz-Montoya, J. G.; Lopez, E. O.; Baena-Moncada, A. M. Advances in the design and application of transition metal oxide-based supercapacitors. *Open Chem.* **2021**, *19*, 709−725.
(38) Afif, A.; Rahman, S. M.; Tasfiah Azad, A.; Zaini, J.; Islan, M. A.; Azad, A. K. Advanced materials and technologies for hybrid supercapacitors for energy storage−a review. *J. Energy Storage* **2019**, *25*, 100852.
(39) Kalantar-zadeh, K.; Vijayaraghavan, A.; Ham, M. H.; Zheng, H.; Breedon, M.; Strano, M. S. Synthesis of Atomically Thin WO_3 Sheets from Hydrated Tungsten Trioxide. *Chem. Mater.* **2010**, *22*, 5660−5666.
(40) Khan, H.; Zavabeti, A.; Wang, Y.; Harrison, C. J.; Carey, B. J.; Mohiuddin, M.; Chrimes, A.; De Castro, I. A.; Zhang, B. Y.; Sabri, Y. M.; Bhargava, S. K.; Ou, J. Z.; Daeneke, T.; Russo, S. P.; Li, Y.; Kalantar-zadeh, K. Quasi physisorptive two dimensional tungsten oxide nanosheets with extraordinary sensitivity and selectivity to NO_2. *Nanoscale* **2017**, *9*, 19162−19175.
(41) Le, P. A.; Nguyen, V. T.; Le, V. Q.; Lu, Y. C.; Huang, S. Y.; Sahoo, S. K.; Chu, Y. H.; Wei, K. H. One-Step Surface-Plasma-Induced Exfoliation of the Graphite/WS_2 Bilayer into Homogeneous Two-Dimensional Graphene/WS_2 Nanosheet Composites as Catalysts for the Hydrogen Evolution Reaction. *ACS Appl. Energy Mater.* **2021**, *4*, 5143−5154.
(42) Le, P. A.; Nguyen, V. T.; Yen, P. J.; Tseng, T. Y.; Wei, K. H. A new redox phloroglucinol additive incorporated gel polymer electrolyte for flexible symmetrical solid-state supercapacitors. *Sustain. Energy Fuels* **2019**, *3*, 1536−1544.
(43) Le, P. A.; Nguyen, V. T.; Sahoo, S. K.; Tseng, T. Y.; Wei, K. H. Porous carbon materials derived from areca palm leaves for high performance symmetrical solid-state supercapacitors. *J. Mater. Sci.* **2020**, *55*, 10751.
(44) Kohn, W.; Sham, L. J. Self-Consistent Equations Including Exchange and Correlation Effects. *Phys. Rev.* **1965**, *140* (4A), A1133−A1138.
(45) Hohenberg, P.; Kohn, W. Inhomogeneous Electron Gas. *Phys. Rev.* **1964**, *136* (3B), B864−B871.
(46) Perdew, J. P.; Wang, Y. Accurate and simple analytic representation of the electron-gas correlation energy. *Phys. Rev. B* **1992**, *45*, 13244.
(47) Perdew, J. P.; Burke, K.; Ernzerhof, M. Generalized Gradient Approximation Made Simple. *Phys. Rev. Lett.* **1996**, *77*, 3865.
(48) Szymanski, J. T.; Roberts, A. C. The crystal structure of tungstite, $WO_3.H_2O$. *Can. Mineral.* **1984**, *22* (4), 681−688.
(49) Chen, L.; Mashimo, T.; Okudera, H.; Iwamoto, C.; Omurzak, E. Synthesis of WO3●H2O nanoparticles by pulsed plasma in liquid. *RSC Adv.* **2014**, *4* (54), 28673−28677.
(50) Wang, P.; Huang, B.; Qin, X.; Zhang, X.; Dai, Y.; Whangbo, M. H. Ag/AgBr/$WO_3.H_2O$: Visible-light photocatalyst for bacteria destruction. *Inorg. Chem.* **2009**, *48* (22), 10697−10702.
(51) Nayak, A. K.; Sohn, Y.; Pradhan, D. Facile Green Synthesis of $WO_3.H_2O$ Nanoplates and WO_3 Nanowires with Enhanced Photoelectrochemical Performance. *Cryst. Growth Des* **2017**, *17* (9), 4949−4957.
(52) Aslam, I.; Hassan Farooq, M.; Iqbal, M. W.; Boddula, R.; Abid, M.; Ashfaq, M.; Ghani, U. Synthesis of $WO_3.H_2O$ spherical particles for efficient photocatalytic properties under visible light source. *Mater. Sci. Energy Technol.* **2019**, *2* (2), 187−193.
(53) Ma, L.; Zhou, X.; Xu, L.; Xu, X.; Zhang, L.; Ye, C.; Luo, J.; Chen, W. Hydrothermal preparation and supercapacitive performance of flower-like $WO_3.H_2O$/reduced graphene oxide composite. *Colloids Surf., A* **2015**, *481*, 609−615.
(54) Gupta, S. P.; Nishad, H. H.; Chakane, S. D.; Gosavi, S. W.; Late, D. J.; Walke, P. S. Phase transformation in tungsten oxide nanoplates as a function of post-annealing temperature and its electrochemical in fluence on energy storage. *Nanoscale Adv.* **2020**, *2*, 4689−4701.
(55) Szkoda, M.; Trzcinski, K.; Trykowski, G.; Łapinski, M.; Lisowska-Oleksiak, A. Influence of alkali metal cations on the photoactivity of crystalline and exfoliated amorphous WO_3−photointercalation phenomenon. *Appl. Catal., B* **2021**, *298*, 120527.

https://doi.org/10.1021/acsomega.1c06150
ACS Omega 2022, 7, 10115−10126

(56) Nguyen, N. T.; Le, P. A.; Phung, V. B. T. Biomass-derived activated carbon electrode coupled with a redox additive electrolyte for electrical double-layer capacitors. *J. Nanopart. Res.* **2020**, *22*, 371.
(57) Nguyen, N. T.; Le, P. A.; Phung, V. B. T.; Facile green synthesis of carbon quantum dots and biomass-derived activated carbon from banana peels: synthesis and investigation, *Biomass Conv. Bioref.* **2020**. DOI: 10.1007/s13399-020-00839-2.
(58) Sharma, L.; Kumar, P.; Halder, A. Phase and Vacancy Modulation in Tungsten Oxide: Electrochemical Hydrogen Evolution. *ChemElectroChem.* **2019**, *6*, 3420−3428.
(59) Nayak, A. K.; Das, A. K.; Pradhan, D. High Performance Solid-State Asymmetric Supercapacitor using Green Synthesized Graphene−WO_3 Nanowires Nanocomposite. *ACS Sustainable Chem. Eng.* **2017**, *5* (11), 10128−10138.
(60) Lokhande, V.; Lokhande, A.; Namkoong, G.; Kim, J. H.; Ji, T. Charge storage in WO_3 polymorphs and their application as supercapacitor electrode material. *Results Phys.* **2019**, *12*, 2012−2020.
(61) Nguyen, N. T.; Le, P. A.; Phung, T. V. B. Biomass-derived carbon hooks on Ni foam with free binder for highperformance supercapacitor electrode. *Chem. Eng. Sci.* **2021**, *229*, 116053.
(62) Yao, S.; Qu, F.; Wang, G.; Wu, X. Facile hydrothermal synthesis of WO_3 nanorods for photocatalysts and Supercapacitors. *J. Alloys Compd.* **2017**, *724*, 695−702.
(63) Shinde, P. A.; Lokhande, A. C.; Chodankar, N. R.; Patil, A. M.; Kim, J. H.; Lokhande, C. D. Temperature dependent surface morphological modifications of hexagonal WO_3 thin films for high performance supercapacitor application. *Electrochim. Acta* **2017**, *224*, 397−404.
(64) Szkoda, M.; Zarach, Z.; Trzciński, K.; Trykowski, G.; Nowak, A. P. An Easy and Ecological Method of Obtaining Hydrated and Non-Crystalline WO_{3-X} for Application in Supercapacitors. *Materials* **2020**, *13*, 1925.
(65) Hai, Z.; Karbalaei Akbari, M.; Wei, Z.; Xue, C.; Xu, H.; Hu, J.; Zhuiykov, S. Nano-thickness dependence of supercapacitor performance of the ALD-fabricated two-dimensional WO_3. *Electrochim. Acta* **2017**, *246*, 625−633.
(66) Chu, J.; Lu, D.; Wang, X.; Wang, X.; Xiong, S. WO_3 nanoflower coated with graphene nanosheet: Synergetic energy storage composite electrode for supercapacitor application. *J. Alloys Compd.* **2017**, *702*, 568−572.
(67) Lokhande, V.; Lokhande, A.; Namkoong, G.; Kim, J. H.; Ji, T. Charge storage in WO_3 polymorphs and their application as supercapacitor electrode material. *Results Phys.* **2019**, *12*, 2012−2020.
(68) Tauc, J.; Grigorovici, R.; Vancu, A. Optical properties and electronic structure of amorphous germanium. *Phys. Status Solidi* **1966**, *15*, 627−637.

https://doi.org/10.1021/acsomega.1c06150
ACS Omega 2022, 7, 10115−10126